Lithium mobility in the NASICON-type compound $LiTi_2(PO_4)_3$ by nuclear magnetic resonance and impedance spectroscopies

1996 J. Phys.: Condens. Matter 8 5355

(http://iopscience.iop.org/0953-8984/8/29/011)

J. Phys.: Condens. Matter **8** (1996) 5355–5366. Printed in the UK

Lithium mobility in the NASICON-type compound $LiTi_2(PO_4)_3$ by nuclear magnetic resonance and impedance spectroscopies

Miguel A París, Ana Martínez-Juárez, José M Rojo and Jesús Sanz

Instituto de Ciencia de Materiales de Madrid (Consejo Superior de Investigaciónes Científicas), Cantoblanco, 28049 Madrid, Spain

Received 31 January 1996

Abstract. Lithium mobility in $LiTi_2(PO_4)_3$ has been followed by ^7Li NMR and impedance spectroscopies. From this analysis, three stages have been distinguished.

(1) Below 230 K, lithium occupies preferentially the octahedral M_1 sites of the NASICON structure.

(2) Between 230 and 330 K, a low correlated and thermally activated lithium motion, with $E_a = 0.47$ eV, is operating, as deduced from both techniques.

(3) Above 330 K, the activation energy decreases and a more extended lithium ionic motion is established. As the lithium mobility increases, progressive occupation of the eight-coordinated M_2 sites is deduced from NMR data.

1. Introduction

The framework of NASICON-type materials $LiM_2(PO_4)_3$, M = Ti, Ge, Zr, . . ., is built up by $M_2(PO_4)_3$ units in which two MO_6 octahedra are linked to three PO_4 tetrahedra by sharing oxygen atoms [1, 2]. The usual symmetry is rhombohedral $R\bar{3}c$, although in several cases (M = Zr or Sn) a monoclinic distortion has been found [3–5]. The Li^+ ions can occupy two different sites [6]: firstly M_1 sites, surrounded by six oxygens atoms and located at an inversion centre, and secondly M_2 sites, surrounded by eight oxygen atoms and disposed around the ternary axis of the structure. Both sites alternate along the conduction channels which form a three-dimensional network. In the $LiTi_2(PO_4)_3$ compound, the distribution of Li^+ ions over the two crystallographic sites is not known but, for the related compositions $Li_{1+x}Ti_{2-x}In_x(PO_4)_3$, with $x = 0.12$ and 0.15, a preferential occupation of M_1 sites at room temperature has been reported [7]. For lithium contents close to that of the composition $Li_3Ti_2(PO_4)_3$, Li^+ ions occupy both types of site, but some controversy about its relative occupation still remains [8, 9].

In general, $LiM_2(PO_4)_3$ compounds are good lithium ion conductors, and the lithium mobility is strongly affected by the nature of the M(IV) cation [10–17]. $LiTi_2(PO_4)_3$ is one of the best ionic conductors of this family. However, determination of bulk conductivity in powder samples is often hindered by the grain boundary response. In order to minimize the last contribution, different thermal sintering treatments and sample preparation procedures have been tried [10–16]. Moreover, the use of the AC impedance measurements allows differentiation of both contributions as a function of frequency. Finally, NMR spectroscopy allows the study of the lithium mobility inside the grains [18, 19] without the limiting effect mentioned above.

0953-8984/96/295355+12$19.50

In this work, NMR and impedance spectroscopies have been used to study the lithium mobility in the rhombohedral $LiTi_2(PO_4)_3$ phase. For that, the dependences of the ^7Li NMR spectra, the spin–spin relaxation time T_2 and the spin–lattice relaxation times T_1 on the sample temperature have been determined. These data have been compared with those deduced for bulk and grain boundary conductivities deduced from impedance measurements. From this comparison, we have identified three different stages in which the location and mobility of Li ions change with temperature.

2. Experimental details

The sample was prepared [20] by calcination at increasing temperatures in the range 573–1373 K of a stoichiometric mixture of Li_2CO_3, $(NH_4)_2H(PO_4)_3$ and TiO_2. The x-ray diffraction pattern of the sample, corresponding to a single phase, coincides with those previously reported by other workers [10–17, 20] and was indexed on the basis of a rhombohedral $R\bar{3}c$ lattice.

Electrical conductivity measurements were carried out by the complex impedance method in a 1174 Solartron frequency response analyser. Autocoherent pellets (of about 6 mm diameter and 1 mm thickness) were obtained in the last stage of the preparation process. Gold electrodes were deposited on the two faces of the pellets by vacuum evaporation. The frequency range used was 10^{-1}–10^5 Hz. The measurements were carried out at different temperatures in heating and cooling runs with the pellet under a nitrogen flow.

The ^7Li NMR spectra were recorded with a SXP 4/100 Bruker spectrometer. The frequency used was 31.01 MHz, which corresponds to an external magnetic field of 1.87 T. The number of accumulations was chosen in the range 100–200. A $\pi/2$ pulse of 3 μs and a period between successive accumulations higher than $5T_1$ was selected for each temperature. The experiments were carried out between 100 and 530 K.

When the intrinsic width of the central line was higher than the inhomogeneity of the external magnetic field, the T_2-values were obtained from single-pulse experiments [21]; T_2^{-1}-values were calculated as 0.6π times the full width at half-height (FWHH) for a Gaussian line and as π times FWHH for a Lorentzian line. In lines of intermediate shape, an average of the aforementioned values was used. When the intrinsic linewidth was of the same order as or smaller than the field inhomogeneity, T_2^{-1}-values were determined by using the Meiboom–Gill modification of the Carr–Purcell sequence (CPMG) [21]: $(\pi/2)_{x'}$–τ–$[(\pi)_{y'}$–τ–$(\pi)_{y'}]^n$. This sequence leads to the cancellation of the effect of external magnetic field inhomogeneities and permits determination of the true T_2 relaxation times. The T_1-values at each temperature were determined by using the classical π–τ–$\pi/2$ sequence [21]. For that, recovery of experimental magnetization was fitted to the exponential function

$$M(\tau) = M_0[1 - 2\exp(-(\tau - t_0)/T_1)] \tag{1}$$

where the spin–lattice relaxation time T_1, the thermal equilibrium magnetization M_0 and the time t_0 were considered to be free parameters in a least-squares fitting procedure.

3. Results

3.1. Impedance spectroscopy

The imaginary part ϵ'' of the permittivity versus angular frequency ($\omega = 2\pi\nu$) for different temperatures is shown in figure 1(*a*). At 148 K a broad peak is clearly observed. Above

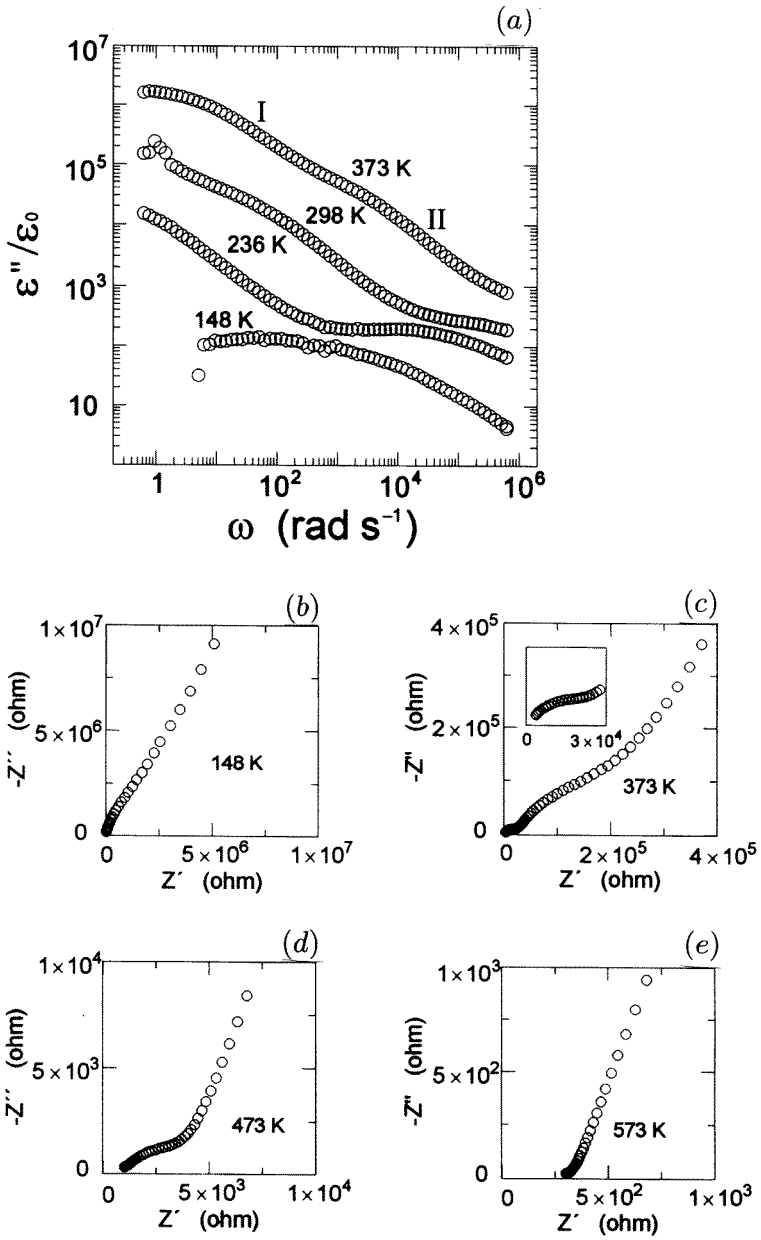

Figure 1. (*a*) Frequency dependence of the imaginary permittivity measured at different temperatures. (*b*)–(*e*) The complex impedance plots (imaginary Z'' versus real Z') measured at increasing temperatures. The inset for 373 K shows the high-frequency arc on an expanded scale.

200 K a strong low-frequency dispersion that is superimposed on the loss peak becomes dominant. At 373 K, two dispersive regimes (I and II) with similar slopes are observed. Another strong low-frequency dispersion is found for the real part of the permittivity but it is not shown in this paper.

The impedance plots (imaginary part $-Z''$ versus real part Z') obtained at different temperatures are shown in figures 1(*b*)–1(*e*). At 148 K the plot shows no arcs. At a higher temperature (373 K), two arcs and spike are clearly observed. When the temperature increases, the arcs disappear progressively from the spectra, first the high-frequency arc (473 K) and then the low-frequency arc (573 K). Above the last temperature, only the spike is detected. According to the data reported for ceramic materials [22, 23], the high-frequency arc is ascribed to the grain interior response while the low-frequency arc is assigned to the grain boundary response. The magnitudes of the capacitance associated with high-frequency and low-frequency arcs are of the order of 100 pF and 10 nF, respectively. The observed spike is ascribed to the Li^+ blocking response at the surface of the electrodes.

The plots of conductivity σ versus frequency ω at different temperatures (figure 2(*a*)) show two plateaux. The plateau at low frequencies (I) corresponds to the total DC conductivity of the pellet and that at higher frequencies (II) to the DC conductivity of the grain interior. At 298 K, in the high-frequency range a small dispersive regime (III) corresponding to the AC conductivity of the grain interior is also observed. The DC values corresponding to grain interior and grain boundary contributions have been deduced at each temperature by fitting the experimental data with the combination of two expressions of the type [24]

$$\sigma = \sigma_{DC} + A\omega^n. \tag{2}$$

The terms σ_{DC} and $A\omega^n$ account for the DC and AC conductivities, respectively. At 473 and 573 K the dispersive regimes (IV) at low frequencies correspond to the electrode blocking effect.

The temperature dependence of the DC conductivity is plotted in an Arrhenius fashion in figure 2(*b*). The values corresponding to the grain interior (full circles) and grain boundary (open triangles) produce a straight line. The total conductivity (open circles) shows two linear dependences with a crossover temperature at 520 K. This feature has been also observed by other workers [16] but the DC values are quite different. By fitting the experimental data with a $\sigma = \sigma_0 \exp(-E_a^\sigma / kT)$ expression, the activation energy E_a^σ and pre-exponential factor σ_0 for the grain interior, grain boundary and total conductivity have been deduced (table 1).

Table 1. Activation energy E_a^σ and pre-exponential factor σ_0 for the Arrhenius plots in figure 2(*b*).

	E_a^σ (eV)	$\log_{10}\sigma_0$ (Ω^{-1} cm^{-1})
Grain interior conductivity	0.48 ± 0.01	1.67 ± 0.02
Grain boundary conductivity	0.69 ± 0.02	3.58 ± 0.04
Total conductivity, $T < 520$ K	0.66 ± 0.01	3.02 ± 0.04
Total conductivity, $T > 520$ K	0.36 ± 0.02	0.19 ± 0.02

3.2. NMR spectroscopy

The ^{7}Li NMR spectra ($I = 3/2$) (figure 3(*a*)) are formed by a central line ($-1/2 \rightarrow 1/2$ transition) and two satellite lines ($1/2 \rightarrow 3/2$, $-3/2 \rightarrow -1/2$ transitions). The satellites are associated with the interaction of the quadrupolar moment of the nuclei with the electric field gradient of the crystal at the structural site (electric quadrupolar interaction [25]). The

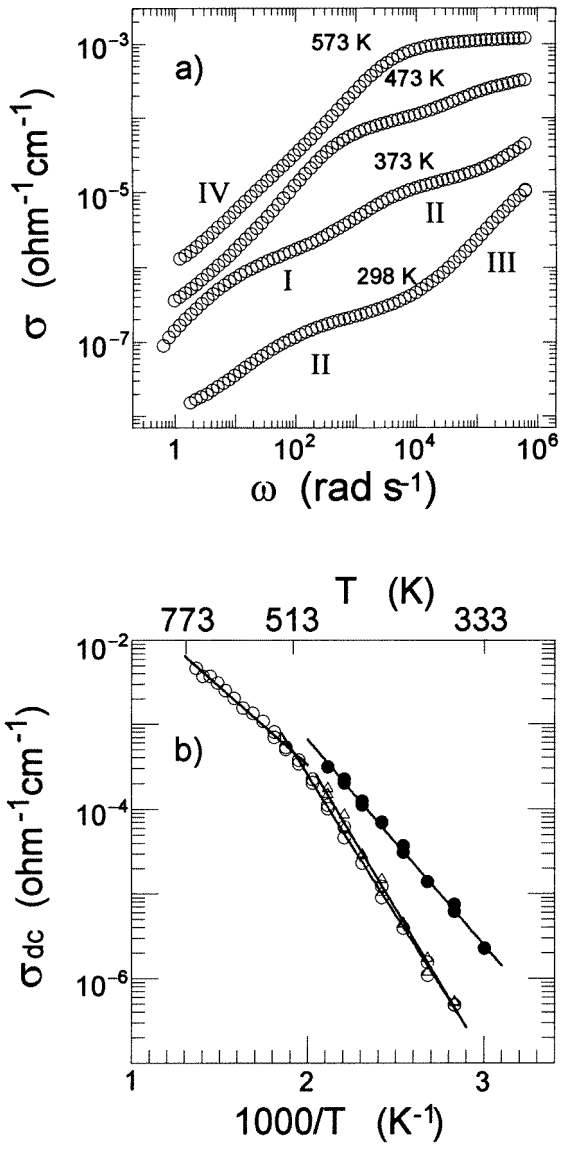

Figure 2. (*a*) Real part of conductivity versus frequency at different temperatures. (*b*) Temperature dependence of DC conductivity in an Arrhenius plot for the grain interior (●), the grain boundary (△) and the whole of the pellet (○).

observed profile for the outer transitions is a consequence of the random orientations of the crystallites in powder samples. Spectra were fitted with the Bruker WINFIT [26] program, which takes into account first-order quadrupolar interactions. From the fitting of spectra, the asymmetry parameter η, the quadrupolar coupling constant C_Q and the shape and width of the central line were determined for each temperature. η is zero in all cases but C_Q increases with the inverse of temperature (figure 3(*b*)). Below 230 K the increase is very slow but, above this temperature, C_Q increases more rapidly.

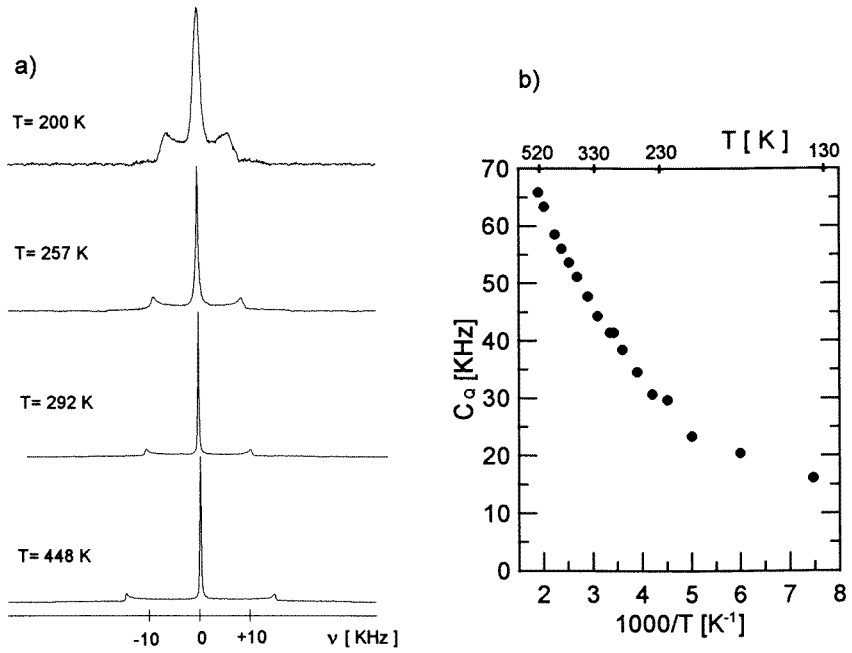

Figure 3. (*a*) ^{7}Li NMR spectra recorded at 31.01 MHz and different temperatures. (*b*) Temperature dependence of the quadrupolar coupling constant C_Q deduced from fitting of the spectra.

The variation in T_2^{-1} deduced from single-pulse experiments versus $1000/T$ is displayed in figure 4(*a*). T_2^{-1} shows a plateau in the 120–230 K range and a decrease above this temperature. In this temperature range the shape of the central line is Gaussian; however, at higher temperatures the line narrows and becomes Lorentzian. In this figure, T_2^{-1}-values obtained by using the CPMG sequence are also plotted. They are considerably lower than those obtained by single-pulse experiments. From the slope of the T_2^{-1} curves, activation energies of 0.24 eV and 0.36 eV have been deduced for T_2^{-1} obtained with single-pulse and CPMG experiments, respectively. Above 300 K, T_2^{-1} obtained by both procedures increases slightly, attains a maximum at 330 K and decreases at higher temperatures.

For the temperature range analysed, the sample displayed a single-exponential spin–lattice relaxation. The temperature dependence of T_1^{-1} is shown in figure 4(*b*). T_1^{-1} shows a plateau below 230 K. Above this temperature, T_1^{-1} increases and at 300 K a maximum is observed. Between 300 and 530 K, T_1^{-1} decreases slightly, displaying a second broad maximum at 470 K. The activation energy deduced from the low-temperature branch of the first maximum is 0.46 eV, but that corresponding to the second maximum is difficult to estimate.

4. Discussion

From the NMR and impedance data, three stages for lithium mobility can be distinguished.

In the first stage, corresponding to temperatures below 230 K, T_2^{-1} and C_Q are almost

constant, indicating that interaction of lithium with its environment almost does not change. In most of the cases analysed in the literature, the constant value of T_1^{-1} is ascribed to a nuclear relaxation induced by paramagnetic impurities in the absence of lithium mobility. The lack of motion is also supported by the electrical data. Thus, only a broad peak of ϵ'' characteristic of dielectric behaviour has been found.

On the other hand, it is known that dipolar interactions between magnetic moments of nuclei broaden the NMR lines and this effect can be used to analyse the environment of nuclei. In our case, the ^{7}Li central line shows a Gaussian shape and the experimental second moment $\Delta\varpi^2$ can be compared with that calculated by using the expression proposed for a rigid lattice in powder samples [25].

$$\Delta\varpi^2 = \tfrac{3}{5}\gamma_I^4\hbar^2 I(I+1)\sum_k \frac{1}{r_{jk}^6} + \tfrac{4}{15}\gamma_I^2\gamma_S^2\hbar^2 S(S+1)\sum_k \frac{1}{r_{jk}^6}. \tag{3}$$

The first term accounts for dipolar interactions between like spins and the second term for those between unlike spins. γ_I and γ_S are the gyromagnetic ratios for the I and S spins. r_{jk} is the distance between interacting spins.

In $LiTi_2(PO_4)_3$ the contribution of the Li–Ti dipolar interaction to $\Delta\varpi^2$ is negligible because of the low γ_S-value of titanium. However, the Li–Li and Li–P dipolar interactions affect notably the value of that parameter. The estimated $\Delta\varpi^2$-values for Li^+ ions occupying the M_1 and M_2 sites in the structure are outlined in table 2 and compared with the experimental $\Delta\varpi^2$-value. It is observed that, for both sites, the Li–P interactions are more important than the Li–Li interactions. Moreover, the good agreement observed between the experimental and the calculated $\Delta\varpi^2$-values for lithium in the M_1 sites indicates the preferential occupancy of that site. Although this result has not been confirmed from diffraction data, it agrees with the preferential occupation of the M_1 site deduced from neutron diffraction data for the related compositions $Li_{1+x}Ti_{2-x}In_x(PO_4)_3$, $x = 0.12$ and 0.15.

Table 2. Estimated second moment, determined on the basis of a rigid lattice, for lithium occupying the M_1 and M_2 sites and experimental second moment calculated from the central line of the ^{7}Li NMR spectra below 230 K.

	$\Delta\varpi^2_{total}$ (G^2)	$\Delta\varpi^2_{Li-P}$ (calc.) (G^2)	$\Delta\varpi^2_{Li-Li}$ (calc.) (G^2)	r_{Li-P} (Å)	r_{Li-Li} (Å)
M_1 site	0.13	0.09	0.04	3.49	6.00
M_2 site	0.33	0.29	0.04	2.58–3.51	6.00
Experimental	0.14				

In the second stage, corresponding to temperatures in the range 230–330 K, lithium moves and its mobility increases with increasing sample temperature. Thus, a decrease in T_2^{-1} and an increase in T_1^{-1} are observed. In addition, the presence of low-frequency dispersions in ϵ' and ϵ'', and the arcs in the impedance plots support clearly the ionic mobility as the dominant factor. An enhancement of the DC conductivity with rising temperature is also found.

The decrease in T_2^{-1} is ascribed to a progressive cancellation of the dipolar interactions produced by the motion of Li^+ ions. This phenomenon (motional narrowing effect) happens when the correlation time τ, i.e. the residence time of Li in the structural sites, is much smaller than the inverse square root $(\Delta\varpi^2)^{-1/2}$ of the static second moment.

The T_1^{-1} relaxation rate is related to the spectral density $J(\omega_0, \tau)$ through the expression [27]

$$\frac{1}{T_1} = C[J(\omega_0, \tau) + 4J(2\omega_0, \tau)] \tag{4}$$

where

$$J(\omega_0, \tau) = \mathrm{Re} \int_{-\infty}^{+\infty} f\left(\frac{t}{\tau}\right) \exp(-\mathrm{i}\omega_0 \tau)\, \mathrm{d}t \tag{5}$$

ω_0 is the Larmor frequency and $f(t/\tau)$ is the autocorrelation function associated with Li^+ motion. The temperature dependence of τ follows the expression $\tau = \tau_0 \exp(E_a/kT)$, E_a being the activation energy and k the Boltzmann constant. In general, the plot of T_1^{-1} versus inverse temperature exhibits a maximum at which the relation $\omega_0\tau \approx 1$ holds. In the case of $LiTi_2(PO_4)_3$, the T_1^{-1} curve exhibits a maximum and a low-temperature branch; however, the high-temperature branch is obscured by the presence of a second relaxation mechanism.

The constant C in equation (4) gives information about the interaction responsible for nuclear relaxation. From the first maximum of the T_1^{-1} curve, a C-value of 2.6×10^{10} s^{-2} has been deduced. If Li–Li and P–Li dipolar interactions were the dominant effect in the spin–lattice relaxation, then $C \approx \Delta\varpi^2$, and a C-value of about 10^7 s^{-2} would be obtained. This value is quite different from that deduced from the T_1^{-1} curve, indicating that dipolar relaxation cannot account for the observed T_1^{-1} values and another relaxation mechanism must be responsible for spin–lattice relaxation. In the case of quadrupolar relaxation [25], $C \approx (2\pi^2/5)(1+\eta^2/3)C_Q^2$, and C-values in the range 1.6×10^9–1.9×10^{10} s^{-2} are obtained. For these calculations, η and C_Q have been taken from the fitting of Li NMR spectra. These C-values are close to that deduced from the maximum of the T_1^{-1} curve, indicating that modulations of the quadrupolar interactions induced by lithium motion are responsible for the T_1^{-1} relaxation rate.

The activation energy deduced from the low-temperature branch of T_1^{-1} (0.46 eV) is different from those obtained from T_2^{-1} data (0.36 and 0.24 eV). As the activation energies deduced from both parameters should be equal, T_2^{-1}-values could be affected by residual field inhomogeneities. In fact, when they are more effectively cancelled by using the CPMG sequence, the activation energy increases from 0.24 eV, obtained with single-pulse experiments, to 0.36 eV and becomes closer to that deduced from T_1^{-1} data (0.46 eV). Therefore, the unique activation energy free of interferences is that deduced from the T_1^{-1} curve.

On the other hand, the DC conductivity corresponding to the motion of Li^+ ions in grain interior and through grain boundaries can be separated in this stage. The values for the grain boundary are lower than for the grain interior and they dominate the total conductivity of the pellet (figure 2(*b*)). The activation energy for the movement of Li^+ ions in the grain interior (0.48 eV) is lower than through the grain boundary (0.69 eV) (table 1). In addition, the activation energy for the grain interior almost coincides with that deduced from the low-temperature branch of the T_1^{-1} curve (0.46 eV).

The observed good agreement between both techniques suggests that the Bloembergen–Purcell–Pound (BPP) [27] model is operating for NMR relaxation and the same activation energy, coincident with that obtained from DC conductivity, should be obtained from the low- and high-temperature branches. On the basis of this model, a low correlation would be present in the motion of Li^+ ions. The weak AC response observed in the σ versus frequency plot (figure 2(*a*)) supports the random-walk mechanism (absence of correlation) for lithium motion.

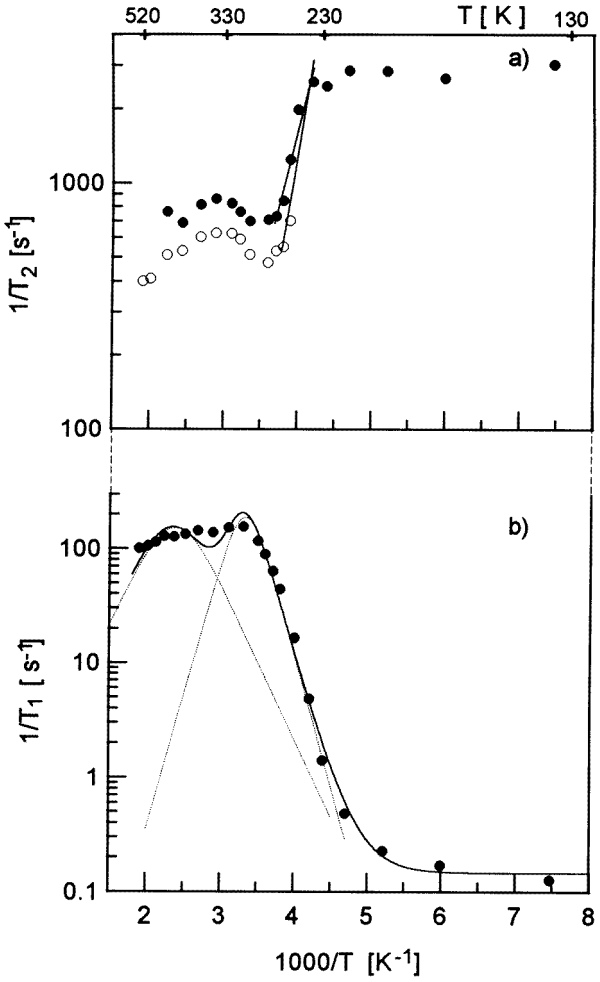

Figure 4. Temperature dependence of the spin–lattice relaxation time T_1^{-1} and the spin–spin relaxation time T_2^{-1}: (*a*) The T_2^{-1}-values obtained with the CPMG sequence (○) and the T_2^{-1}-values obtained with single-pulse experiments (●). (*b*) The T_1^{-1}-values obtained at 31.01 MHz for each temperature (●), the fitting of these values on the basis of two BPP relaxation mechanisms (——) and the contribution of each mechanism to the spin–lattice relaxation rate (· · · · · ·) (see the discussion for details).

Between 230 and 330 K, an increase in C_Q with increasing sample temperature is also observed. This tendency, which is contrary to that expected for thermal expansion of the unit cell, points to a change in the lithium environment. In particular, the increase in ion mobility should favour the progressive occupation of the M_2 sites at the expense of the initially occupied M_1 sites. Preliminary calculations of electric field gradient for both sites in $LiTi_2(PO_4)_3$ have shown that the quadrupolar interaction is higher in the less symmetric M_2 site. Then, as the Li motion averages the quadrupolar interactions existing in the two crystallographic sites, it could produce the observed increase in C_Q.

Finally, a third stage in the lithium mobility can be distinguished when the sample is heated above 330 K.

T_2^{-1} shows a slight maximum at about 350 K and above this temperature an additional decrease. The increase in the residence time in the M_2 sites could explain this fact; the Li–P dipolar interaction is higher in the M_2 site than in the M_1 site, producing a slow increase in T_2^{-1}-values. An additional enhancement of the lithium mobility in the third stage would cancel this residual interaction and cause the new decrease in T_2^{-1}.

The experimental T_1^{-1} curve cannot be fitted by using a single BPP curve with an activation energy of 0.46 eV, and at least another relaxation mechanism is required. In figure 4(*b*) the fitting of the experimental T_1^{-1} curve by using the following expression is shown:

$$\frac{1}{T_1} = \frac{1}{T_1^{LT}} + \frac{1}{T_1^{HT}} + \frac{1}{T_1^{PAR}} \tag{6}$$

where $(T_1^{LT})^{-1}$ and $(T_1^{HT})^{-1}$ stand for the low-temperature and high-temperature mechanisms, respectively, and $(T_1^{PAR})^{-1}$ is the contribution of paramagnetic impurities, which causes the low-temperature plateau. The expressions used for $(T_1^{LT})^{-1}$ and $(T_1^{HT})^{-1}$ are those predicted by the BPP model:

$$\frac{1}{T_1^i} = C^i \left\{ \frac{\tau_i}{1+(\omega_0\tau_i)^2} + \frac{4\tau_i}{1+4(\omega_0\tau_i)^2} \right\} \tag{7}$$

where $i = LT$ or HT. In these simulations, $(T_1^{PAR})^{-1}$ has been considered independent of temperature. The parameters corresponding to the best fit are displayed in table 3. Deduced τ_0- and E_a-values indicate clearly the existence of two maxima corresponding to two types of lithium mobility; the high-temperature data can be fitted reasonably by a symmetric relaxation curve with a lower activation energy (0.27 eV) than that of the low-temperature data (0.46 eV).

Table 3. Parameters deduced from the fitting of the T_1^{-1} curve by equation (6). See the text for details.

C^{LT} (s^{-2})	τ_0^{LT} (s)	E_a^{LT} (eV)	C^{HT} (s^{-2})	τ_0^{HT} (s)	E_a^{HT} (eV)	$(T_1^{PAR})^{-1}$ (s^{-1})
2.6×10^{10}	6.4×10^{-17}	0.46	2.1×10^{10}	1.9×10^{-12}	0.27	0.14

The presence of a different relaxation mechanism in the third stage is also supported by the conductivity data. Thus, a new Arrhenius dependence for the total conductivity with a low activation energy (0.37 eV) is observed. Above 490 K the DC conductivity for the grain interior and grain boundary cannot be resolved; however, the total conductivity cannot be explained on the basis of the same Arrhenius dependences used for the grain interior and grain boundary in the second stage. Then, it seems that both contributions change at about 513 K and lithium motion becomes easier in this stage. The comparison between activation energies deduced in this stage from NMR and conductivity data is difficult owing to the low resolution of the two peaks in the T_1^{-1} curve and the impossibility of resolving the grain interior contribution to the total conductivity.

On the other hand, C_Q displays a more marked increase with increasing temperature than that observed in the second stage. This points to the presence of a fast exchange of lithium between M_1 and M_2 sites and an additional decrease in the residence time of lithium in the M_1 sites. However, the equal occupation probabilities of both types of site, compatible with the $R\bar{3}c$ symmetry, is not reached in the range of temperatures analysed as a constant C_Q value should have been obtained.

As significant changes have not been observed by XRD in the third stage, all observations support the existence of a more extended lithium motion in the framework of the $LiTi_2(PO_4)_3$. This observation agrees with those reported for the $LiZr_2(PO_4)_3$ and $Li_3In_2(PO_4)_3$ compounds in which a superionic state has been proposed [28, 29] for the same range of temperatures. From this fact, a high-mobility state could be a common point for NASICON-type compounds. However, the analysis of structural causes that produces this state requires additional investigations that are beyond the scope of this work.

5. Conclusions

From the NMR and conductivity study of the $LiTi_2(PO_4)_3$, three stages on lithium mobility have been deduced.

(1) Below 230 K, lithium ions do not move. From the analysis of the second moment of the central line of the NMR spectra it has been deduced that lithium occupies the M_1 sites preferentially.

(2) In the second stage, corresponding to temperatures between 230 and 330 K, the lithium mobility increases. Correlation between lithium ions in their motion is low and the same activation energy (0.47 eV) has been obtained from spin–lattice relaxation and DC conductivity data. In this stage, occupation of M_2 sites by Li increases with increasing temperature.

(3) In the third stage an extended lithium motion has been observed, above 330 K. From both techniques, lower activation energies for lithium motion (0.27 and 0.37 eV) have been deduced. In this stage, occupation of the M_1 sites and occupation of the M_2 sites become more similar.

References

[1] Sljukic M, Matkovic B, Prodic B and Anderson D 1969 *Z. Kristallogr.* **130** 148
[2] Hong H Y-P 1976 *Mater. Res. Bull.* **11** 173
[3] Sudreau F, Petit D and Boilot J P 1989 *J. Solid State Chem.* **83** 78
[4] Alamo J and Rodrigo J L 1989 *Solid State Ionics* **32–3** 70
[5] Martínez A, Rojo J M, Iglesias J E and Sanz J 1995 *Chem. Mater.* **7** 1857
[6] Goodenough J B, Hong H Y-P and Kafalas J A 1976 *Mater. Res. Bull.* **11** 203
[7] Tran Qui D, Hamdoune S, Soubeyroux J L and Prince E 1988 *J. Solid State Chem.* **72** 309
[8] Delmas C, Nadiri A and Soubeyroux J L 1988 *Solid State Ionics* **28–30** 419
[9] Wang S and Hwu S-J 1991 *J. Solid State Chem.* **90** 337
[10] Winand J M, Rulmont A and Tarte P J 1991 *J. Solid State Chem.* **93** 341
[11] Subramanian M A, Subramanian R and Clearfield A 1986 *Solid State Ionics* **18–19** 562
[12] Yong Y and Wenqin P 1990 *Mater. Res. Bull.* **25** 841
[13] Aono H, Sugimoto E, Sadaoka Y, Imanaka N and Adachi G 1990 *Solid State Ionics* **40–1** 38
[14] Aono H, Sugimoto E, Sadaoka Y, Imanaka N and Adachi G 1991 *Solid State Ionics* **47** 257
[15] Ando Y, Hirose N, Kuwawo J, Kato M and Ohtsuka H 1991 *Ceramics Today—Tomorrow's Ceramics* (Amsterdam: Elsevier) p 2245
[16] Aono H, Sugimoto E, Sadaoka Y, Imanaka N and Adachi G 1993 *J. Electrochem. Soc.* **140** 1827
[17] Kuwano J, Sato N, Kato M and Takano K 1994 *Solid State Ionics* **70–1** 332
[18] Prigge C, Müller-Warmuth W, Gocke E and Schölhorn R 1993 *Solid State Ionics* **62** 143
[19] Brinkmann D, Mail M, Roos J, Messer R and Birli H 1982 *Phys. Rev.* B **26** 4810
[20] Masse R 1970 *Bull. Soc. Fr. Mineral. Cristallogr.* **93** 500
[21] Fukushima E and Roeder S B W 1981 *Experimental Pulse NMR (A Nuts and Bolts Approach)* (Reading MA: Addison-Wesley)
[22] Bruce P G and West A R 1983 *J. Electrochem. Soc.* **130** 662
[23] Macdonald J R 1987 *Impedance Spectroscopy* (New York: Wiley) p 217

[24] Jonscher A K 1983 *Dielectric Relaxation in Solids* (London: Chelsea Dielectrics Press) p 223
[25] Abragam A 1961 *The Principles of Nuclear Magnetism* (Oxford: Oxford University Press)
[26] Massiot D 1993 *WINFIT program* © Bruker-Franzen Analytik GmbH
[27] Bloembergen N, Purcell E M and Pound R V 1948 *Phys. Rev.* **73** 679
[28] Petit D, Colomban Ph, Collin G and Boilot J P 1986 *Mater. Res. Bull.* **21** 365
[29] Pronin S, Sigaryov S E and Vashman A A 1990 *Solid State Ionics* **38** 9